Assimilation of surface observations in a transient marine ice sheet model using an ensemble Kalman filter

Fabien Gillet-Chaulet[1]

[1]Univ. Grenoble Alpes, CNRS, IRD, IGE, F-38000 Grenoble, France

Correspondence: Gillet-Chaulet Fabien (fabien.gillet-Chaulet@univ-grenoble-alpes.fr)

Abstract.

Marine based sectors of the Antarctic Ice Sheet are increasingly contributing to sea level rise. The basal conditions exert an important control on the ice dynamics and can be propitious to instabilities in the grounding line position. Because the force balance is non-inertial, most ice flow models are now equipped with time-independent inverse methods to constrain the basal conditions from observed surface velocities. However, transient simulations starting form this initial state usually suffer from inconsistencies and are not able to reproduce observed trends. Here, using a synthetic flow line experiment, we assess the performance of an ensemble Kalman filter for the assimilation of transient observations of surface elevation and velocities in a marine ice sheet model. The model solves the shallow shelf equation for the force balance and the continuity equation for ice thickness evolution. The position of the grounding line is determined by the floatation criterion. The filter analysis estimates both the state of the model, represented by the surface elevation, and the basal conditions, with the simultaneous inversion of the basal friction and topography. The idealized experiment reproduces a marine ice sheet that is in the early stage of an unstable retreat. Using observation frequencies and uncertainties consistent with current observing systems, we find that the filter allows to accurately recover both the basal friction and topography after few assimilation cycles with relatively small ensemble sizes. In addition it is found that assimilating the surface observations has a positive impact to constrain the evolution of the grounding line during the assimilation window. Using the initialised state to perform century-scale forecast simulations, we show that grounding line retreat rates are in agreement with the reference, however remaining uncertainties in the basal conditions may lead to significant delays in the initiation of the unstable retreat. These results are encouraging for the application to real glacial systems.

1 Introduction

Despite recent significant improvements in ice-sheet models, the projected magnitude and rate of the Antarctic and Greenland ice sheets contribution to 21st century sea-level rise (SLR) remains poorly constrained (Church et al., 2013). Improving our

ability to model the century-scale magnitude and rates of mass loss from marine ice sheets remains a key scientific objective (Scambos et al., 2017).

Improving SLR estimates requires, amongst others, to correctly model the dynamics of the grounding line (GL), i.e. the line where the ice detaches from its underlying bed and goes afloat on the ocean (Durand and Pattyn, 2015). In the GL vicinity, the

5 stress regime changes from a regime dominated by vertical shearing in the grounded part to a buoyancy driven flow dominated by longitudinal stretching and lateral shearing (Pattyn et al., 2006; Schoof, 2007). Because this transition occurs on horizontal dimensions that are smaller than the typical grid size of large scale ice sheet models, many studies have focussed on the ability of the numerical model to properly simulate grounding line migration using synthetic experiments (e.g. Vieli and Payne, 2005; Durand et al., 2009; Gladstone et al., 2012; Seroussi et al., 2014). Two Marine Ice-Sheet Model Intercomparison Projects

10 (MISMIP) have allowed to identify the minimum requirements to properly resolve GL motion: *(i)* inclusion of membrane stresses and *(ii)* a sufficiently small grid size or a subgrid interpolation of the GL (Pattyn et al., 2012, 2013). These results suggest that, in realistic applications, the numerical error could be reduced below the errors associated with uncertainties in the model initial state, in the model parameters and in the forcings from the atmosphere and ocean.

For obvious reasons of inaccessibility, the basal conditions (topography and friction) are an important source of uncertain-

15 ties. Because of the intrinsic instability of marine ice sheets resting over a seaward up-sloping bed, the resolution of the bed topography in the coastal regions can significantly affect short term ice-sheet forecasts (Durand et al., 2011; Enderlin et al., 2013). Analytical developments have shown that the flux at the grounding line depends on the friction law and its coefficients (Schoof, 2007; Tsai et al., 2015). The sensitivity of model projections to the basal friction has been confirmed by several numerical studies both on synthetic and real applications (Joughin et al., 2010; Ritz et al., 2015; Brondex et al., 2017, 2018). In

20 particular, Brondex et al. (2017) have shown that, for unbuttressed ice sheets, spatially varying friction coefficients can lead to stable GL positions also in up-sloping bed regions.

Uncertainties in the model state and parameters can be reduced by data assimilation (DA). The objective of formal DA methods is to update the model using observations in a framework consistent with the model, the data and their associated uncertainties (Bannister, 2017). Most ice flow models are now equipped with variational methods to constrain the basal condi-

25 tions from surface observations (e.g. MacAyeal, 1993; Vieli and Payne, 2003; Larour et al., 2012; Gillet-Chaulet et al., 2012). However most of the studies perform "snapshot" calibrations, where the inversion is performed at a unique initial time step. The state of the model produced from this calibration is therefore sensitive to inconsistencies between the different datasets. The resulting transient artefacts are usually dissipated during a relaxation period where the model drift from the observations.

Because historic remote sensing data collections are spatially incomplete as well as temporally sparse, most distributed

30 maps are mosaicked, stacked or averaged to maximize the spatial coverage at the expense of the temporal information (Mouginot et al., 2012). However, in the last few years, the development of spaceborne ice-sheet observations has entered a new era with the launch of new satellite missions, considerably increasing the spatial and temporal resolution of surface observations. Because they require linearized versions of the forecast model and of the observation operator, extending the existing variational methods implies important numerical developments (*e.g.* Goldberg et al., 2016; Larour et al., 2016; Hascoët and

35 Morlighem, 2018). In Goldberg and Heimbach (2013), a time-dependent adjoint ice flow model is derived using a source-to-

source algorithmic differentiation software combined with analytical methods. The DA capabilities are illustrated with a suite of synthetic experiments, including the simultaneous inversion of the basal topography and friction from surface observations and the assimilation of transient surface elevations to retrieve initial ice thicknesses. In a real-world application to a region of West Antarctica, they show that assimilating annually resolved observations of surface height and velocities between 2002 and

5   2011 allows to improve the model initial state, giving better confidences in projected committed mass losses (Goldberg et al., 2015). Because of the complexity of the code, Larour et al. (2014) use an operator-overloading approach to generate the adjoint and assimilate surface altimetry observations from 2003 to 2009 to constrain the temporal evolution of the basal friction and surface mass balance of the Northeast Greenland Ice Stream.

Ensemble DA methods, based on the ensemble Kalman filter (EnKF), have been successfull in solving DA problems with

10   large and non-linear geophysical models. Comparative discussions of the performances and advantages of variationnal and ensemble DA methods can be found in, *e.g.* Kalnay et al. (2007) and Bannister (2017). EnKF approximates the state and the error covariance matrix of a system using an ensemble that is propagated forward in time with the model, avoiding the computation of the covariance matrices and the use of linearised or adjoint models. The observations are then assimilated sequentially in time to update the ensemble, using the analysis step of the Kalman Filter. Since the first version introduced by

15   Evensen (1994) many variants have been developped mainly differing in the way the Kalman Filter analysis is rewrited and the analysed error covariance matrix resampled (e.g. Pham et al., 1998; Bishop et al., 2001; Nerger et al., 2012). A review of the most popular EnKFs using common notations can be found in Vetra-Carvalho et al. (2018). Efficient and parallel algorithms have been developed, and because they are independent of the forward model, several open-source toolboxes that implements various EnKFs are now available, e.g. OpenDA (https://www.openda.org), PDAF (http://pdaf.awi.de).

20   As Monte-Carlo methods, EnKFs suffer from under sampling issues as often the size of the ensemble is much smaller than the size of the system to estimate. Localisation and inflation are popular methods to counteract these issues and to increase the stability of the filtering. Because they are based on the original Kalman Filter equations, EnKFs are optimal only for Gaussian distributions and linear models. However the many applications in meteorology and oceanography show that these methods are efficient in practice.

25   In the context of ice-sheet modelling, encouraging results have been obtained by Bonan et al. (2014) for the estimation of the state and basal conditions of an ice-sheet model using the Ensemble Transform Kalman Filter (ETKF, Bishop et al., 2001; Hunt et al., 2007). Using a shallow ice model and synthetic 1D twin experiments, they show that both the basal topography and basal friction can be retrieved with good accuracy from surface observations with realistic noise levels, even for relatively small ensembles. The method has been further developed to assimilate the margin position in a shallow ice model that explicitly

30   tracks the boundaries with a moving mesh method (Bonan et al., 2017).

The purpose of this paper is to explore the performance of ensemble Kalman filtering for the initialisation of a marine ice sheet model that includes GL migration. In particular, we want to address *(i)* the quality of the analysis for the simultaneous estimation of the basal topography and friction in the context of a marine ice sheet that is undergoing an unstable GL retreat, and *(ii)* the effects of the remaining uncertainties for the predictability of GL retreat. The ice flow model and the EnKF used in

35   this study are described in Section 2. To test the DA framework, we define a twin experiment in Section 3. Section 4 presents

the results for both the transient assimilation and the forecasts. Finally, perspectives and challenges for real applications are discussed in Section 5, before concluding remarks.

2 Methods

2.1 Ice flow model

5 The gravity-driven free surface flow of ice is solved using the finite-element ice flow model Elmer/Ice (Gagliardini et al., 2013).

For the force balance, we solve the shelfy-stream approximation (SSA) equation (MacAyeal, 1989) in one horizontal dimension. This is a vertically integrated model that derives from the Stokes equations for small aspect ratio and basal friction. In 1D, this leads to the following equation for the horizontal velocity field u

$$\frac{\partial}{\partial x}\left(4\bar{\eta}H\frac{\partial u}{\partial x}\right) - \tau_b = \rho_i g H \frac{\partial z_s}{\partial x} \tag{1}$$

10 whith ρ_i the ice density, g the gravity norm, $H = z_s - z_b$ the ice thickness with z_s and z_b the top and bottom surface elevations, respectively. Using the Glen's constitutive flow law, the vertically averaged effective viscosity $\bar{\eta}$ is given by

$$\bar{\eta} = \frac{1}{H}\int\limits_{z_b}^{z_s}\frac{1}{2}A^{-1/n}D_e^{(1-n)/n}\mathrm{d}z \tag{2}$$

where D_e is the second invariant of the strain-rate tensor, equal here to $D_e^2 = (\partial u/\partial x)^2$, A is the rate factor and n is the creep exponent, taken equal to the usual value $n = 3$ in the following. The basal friction τ_b is null under floating ice and is represented

15 with the non-linear Weertman friction law for grounded ice

$$\tau_b = Cu^m \tag{3}$$

with C and m the friction coefficient and exponent, respectively. In the following, we use the classical power law with $m = 1/n = 1/3$. When in contact with the ocean, the ice is assumed to be in hydrostatic equilibrium. The floating condition is evaluated directly at the integration points and τ_b in Eq. (1) is set to 0 wherever ice is floating (Seroussi et al., 2014).

20 Because of the hydrostatic equilibrium, the ice sheet topography is fully defined by the bed elevation b and only one prognostic variable. Equation (1) is then coupled with the vertically integrated mass conservation equation for the evolution of the ice thickness H

$$\frac{\partial H}{\partial t} + \frac{\partial(uH)}{\partial x} = a_s - a_b \tag{4}$$

with a_s the surface accumulation rate and a_b the basal melt rate. The free surfaces z_s and z_b are obtained from the floating

25 condition which, for z_s, using a constant sea level $z_{sl} = 0$, gives

$$\begin{cases} z_s = b + H & \text{for } H \geq -b\dfrac{\rho_w}{\rho_i} \\ z_s = H\left(1 - \dfrac{\rho_i}{\rho_w}\right) & \text{otherwise} \end{cases} \tag{5}$$

with ρ_w the sea water density.

2.2 Data Assimilation

For the assimilation, we use the Error Subspace Ensemble Transform Kalman Filter (ESTKF, Nerger et al., 2012). Originally derived from the singular evolutive interpolated Kalman filter (SEIK, Pham et al., 1998), ESTKF leads to the same ensemble transformations as the ETKF but at a slightly lower computational cost. In practice we use the local version of the filter implemented in PDAF (http://pdaf.awi.de Nerger et al., 2005) and coupled to Elmer/Ice in an offline mode. This section outlines the ESTKF algorithm.

As an EnKF, ESTKF approximates the state x^k and the error covariance matrix $\mathbf{P}_k$ of a system at time t_k using an ensemble of N_e realisations x_i^k, $i = 1, ..., N_e$. The state vector, of size N_x, contains the prognostic variables and model parameters to be estimated and is approximated by the ensemble mean

$$\bar{x}^k = \frac{1}{N_e} \sum_{i=1}^{N_e} x_i^k \tag{6}$$

while the error covariance matrix is given by

$$\mathbf{P}_k = \frac{1}{N_e} \mathbf{X}'_k \mathbf{X}'^T_k \tag{7}$$

where $\mathbf{X}'_k = (x_1^k - \bar{x}^k, ..., x_{N_e}^k - \bar{x}^k) \in \mathbb{R}^{N_x \times N_e}$ is the ensemble perturbation matrix.

The algorithm can be decomposed in two steps, the *forecast* and the *analysis*. Superscripts ^{f} (resp. ^{a}) denote quantities related to each step respectively. During the forecast, we use the numerical model M_k, assumed perfect in the sequel, to propagate the ensemble from a previous analysis at $t = t_{k-1}$ to $t = t_k$ where new observations are available

$$x_i^{f,k} = M_k(x_i^{a,k-1}) \tag{8}$$

This step allows to propagate the state and the error covariance matrix of the system forward in time. During the analysis the ensemble is updated using the available observations and in the following we will omit the time index ^{k} in the notations as all the analysis is performed at $t = t_k$.

The analysis step is based on the KF equations where the state vector and the covariance matrix are updated using the following equations

$$\begin{cases} \bar{x}^a = \bar{x}^f + \mathbf{K}d \\ \mathbf{P}^a = (\mathbf{I} - \mathbf{K}\mathbf{H})\mathbf{P}^f \end{cases} \tag{9}$$

where

– $d = y - H(\bar{x}^f)$ is the *innovation*,

– y is the vector of observations of size N_y,

– H is the *observation operator*, with the matrix $\mathbf{H}$ the linearised observation operator

– **K** is the *Kalman gain* given by

$$\mathbf{K} = \mathbf{P}^f \mathbf{H}^T (\mathbf{H}\mathbf{P}^f \mathbf{H}^T + \mathbf{R})^{-1} \tag{10}$$

– and **R** is the observation error covariance matrix.

With large models ($N_x >> 1$), it is not possible to form the matrix $\mathbf{P}^f$. ESTKF as other EnKFs, performs the analysis in a low-

5 dimensional subspace, denoted the error subspace, which approximates the full error space. This makes the implementation efficient and tractable for large models. The use of an error subspace is possible because the sample covariance matrix $\mathbf{P}_k \in \mathbb{R}^{N_x \times N_x}$ in Eq. (7) has a rank at most $N_e - 1$. However, the drawback of approximating the covariance matrix by a low-rank matrix is that the analysis will adjust the model state only in this subspace, ignoring errors directions not accounted for by the ensemble (Hunt et al., 2007).

10 To perform the projection onto the error subspace, ESTKF use the deterministic matrix $\mathbf{\Omega} \in \mathbb{R}^{N_e \times N_e - 1}$

$$\Omega_{ij} = \begin{cases} 1 - \dfrac{1}{N_e} \dfrac{1}{\frac{1}{\sqrt{N_e}} + 1} & \text{for } i = j,\ i < N_e \\[2ex] -\dfrac{1}{N_e} \dfrac{1}{\frac{1}{\sqrt{N_e}} + 1} & \text{for } i \neq j,\ i < N_e \\[2ex] -\dfrac{1}{\sqrt{N_e}} & \text{for } i = N_e \end{cases} \tag{11}$$

The basis vectors of the error subspace are then given by

$$\mathbf{L} = \mathbf{X}^f \mathbf{\Omega} \tag{12}$$

where $\mathbf{X}^f = (\boldsymbol{x}_1, ..., \boldsymbol{x}_{N_e}) \in \mathbb{R}^{N_x \times N_e}$

15 Finally, the update step can be written as a single equation for the transformation of **L** to the analysed ensemble $\mathbf{X}^a$ as

$$\mathbf{X}^a = \bar{\mathbf{X}}^f + \mathbf{L}(\bar{\mathbf{W}} + \mathbf{W}) \tag{13}$$

where $\bar{\mathbf{W}}$ is a matrix where the columns are given by the vector

$$\bar{w} = \mathbf{A}(\mathbf{HL})^T \mathbf{R}^{-1} \boldsymbol{d} \tag{14}$$

and

20 $$\mathbf{W} = \sqrt{N_e - 1}\mathbf{C}\mathbf{\Omega}^T \tag{15}$$

The transform matrix $\mathbf{A} \in \mathbb{R}^{N_e - 1 \times N_e - 1}$ is computed as

$$\mathbf{A}^{-1} = \rho(N_e - 1)\mathbf{I} + (\mathbf{HL})^T \mathbf{R}^{-1} \mathbf{HL} \tag{16}$$

and **C** in Eq. 15 is taken as its symmetric square root. Multiplicative covariance inflation is tuned using the *forgetting factor* ρ, with $0 < \rho \leq 1$. By increasing the analysed ensemble spread, inflation is a popular method to counteract the effects of

25 undersampling and enhance the filter robustness.

The product $\mathbf{HL}$ in the equations above is computed, using Eq. (11), as $(\mathbf{HX}^f)\mathbf{\Omega}$. The product $\mathbf{HX}^f$ project each ensemble member in the observation space and can then be computed using the non-linear observation operator applied to each member $H(\boldsymbol{x}_i)$. Further, the multiplication with $\mathbf{\Omega}$ implicitly subtracts the observed ensemble mean leading to consistent formulations for the covariance matrices $\mathbf{P}^f\mathbf{H}^T$ and $\mathbf{HP}^f\mathbf{H}^T$ in Eq. (10) (Houtekamer and Mitchell, 2001). For consistency, the vector

5 $H(\bar{\boldsymbol{x}}^f)$ used for the computation of the innovation $\boldsymbol{d}$ in Eq. (14) is then also computed as the observed ensemble mean. The same linear approximation is made by Hunt et al. (2007) for the derivation of the local ETKF.

Here, we use a local formulation of the filter. The localisation algorithm is based on domain localisation and observation localisation (Hunt et al., 2007). It assumes that observations far from a given location have negligible influence. This effectively drops long-range correlations that may truly exist but, on the other hand, that are unlikely properly estimated with a small

10 ensemble size. In practice, the state vector in each single mesh node is updated independently during a loop through the nodes that can easily be parallelized for numerical efficiency. For each local analysis, only the observations within a given radius r from the current node are used. In addition to avoid an abrupt cut-off, the observation error covariance matrix $\mathbf{R}$ is modified so that the inverse observation variance decreases to zero with the distance from the node using a fifth-order polynomial function which mimics a Gaussian function but has compact support (Gaspari and Cohn, 1999). Because it drops spurious long-range

15 correlations and allows the local analyses to choose different linear combinations of the ensemble members in different regions, localisation implicitly increases the rank of the covariance matrix, leading to a larger dimension of the error subspace, implicitly increasing the effective ensemble size and the filter stability (Nerger et al., 2006; Hunt et al., 2007).

3 Experimental design

To evaluate the performance of the DA framework we perform a twin experiment. In this section we first describe the synthetic

20 reference simulation that will be used to assess the performance of the DA framework. From this reference, we generate a set of synthetic noisy observations that will be used by the assimilation scheme. Finally, we describe the initial ensemble constructed using *a priori* or background informations.

3.1 Reference simulation

We start by building an initial steady marine ice-sheet. The domain extends from $x = 0\,\mathrm{km}$ where we apply a symmetry

25 condition, $u = 0$ in Eq. (1), to $x = 800\,\mathrm{km}$ where we have a fixed calving front. We use 1D linear elements with a uniform mesh resolution of $200\,\mathrm{m}$, leading to 4001 mesh nodes.

Following Durand et al. (2011), we generate a synthetic bed geometry that reproduces a typical large-scale overdeepening with some small scale roughness. The bed $b = b_{trend} + b_r$ is the sum of a general trend b_{trend} defined as

$$b_{trend} = \begin{cases} -1100 + x & \text{for } x \leq 450\,\mathrm{km} \\ -650 - 5(x - 450) & \text{for } x > 450\,\mathrm{km} \end{cases} \tag{17}$$

and a roughness signal b_r that is computed at $200\,\mathrm{m}$ resolution using an iterative random mid-point algorithm with a prescribed fractal dimension of 1.3. The resulting bed is shown in Fig. 1.

For the basal friction, we use a synthetic sinusoidal function with two wavelengths for C $(\mathrm{MPa}\,\mathrm{m}^{-\frac{1}{3}}\,\mathrm{a}^{-\frac{1}{3}})$

$$C = 0.020 + 0.015\sin(5\frac{2\pi x}{L})\sin(100\frac{2\pi x}{L}) \tag{18}$$

with $L = 800\,\mathrm{km}$ (Fig. 2).

Using an uniform ice rigidity $B = (2A)^{-1/n} = 0.4\,\mathrm{MPa}\,\mathrm{a}^{\frac{1}{3}}$, we grow an ice sheet to steady state using a uniform surface accumulation $a_s = 0.5\,\mathrm{m}\,\mathrm{a}^{-1}$ and no basal melting $a_b = 0$. The steady state GL is located at $x = 440\,\mathrm{km}$, just downstream of the region of overdeepening (Fig. 1).

At $t = 0$, we instantaneously decrease the ice rigidity to $B = 0.3\,\mathrm{MPa}\,\mathrm{a}^{\frac{1}{3}}$, keeping all the other parameters constant. This initial perturbation induce an acceleration, a thinning and a retreat of the GL. The model is then run for 200 years. After a short stabilisation at $x = 437.2\,\mathrm{km}$ between $t = 13\,\mathrm{a}$ and $t = 32\,\mathrm{a}$, the GL retreats at a rate of approximately $1\,\mathrm{km}\,\mathrm{a}^{-1}$ during the following 100 years, then the rate decreases as the GL enters an area of down-slopping bed (Fig. 1). The retreat rate shows small variations associated with spatial variations of the topography and basal friction.

3.2 Synthetic Observations

From the reference run, we generate synthetic noisy observations that are typical of the resolution and performance of actual observing systems.

For the bed, we mimic an airborne radar survey conducted perpendicular to the ice flow with an along flow resolution of approximately $15\,\mathrm{km}$. For this, we randomly select 54 locations between $x = 0$ and $x = 800\,\mathrm{km}$, and then linearly interpolate the true bed and add a random uncorrelated Gaussian noise with a standard deviation of $20\,\mathrm{m}$ (Fig. 2).

We assume that the surface elevation and velocities are observed at an annual resolution at each mesh node. We then add an uncorrelated Gaussian noise with a standard deviation of $10\,\mathrm{m}$ for the surface elevation and $20\,\mathrm{m}\,\mathrm{a}^{-1}$ for the velocity. The most recent velocity products are now posted with a monthly to annual resolution (Mouginot et al., 2017; Joughin et al., 2018). The reported uncertainty for individual velocity estimates using the 6- and 12-day image pairs from the Sentinel 1A/B satellites is 6.2 and $17.5\,\mathrm{m}\,\mathrm{a}^{-1}$ for the two horizontal velocity components in stable conditions; however this could be underestimated in the coastal areas. For the surface elevation, the spatial and temporal resolution as well as the coverage and uncertainty will depend on the sensors. The ArcticDEM (http://arcticdem.org) is a collection of openly available digital surface models derived from satellite imagery and posted at $2-\mathrm{m}$ spatial resolution. After co-registration, a standard deviation ranging from 2 to $4\,\mathrm{m}$ has been reported for the uncertainty of elevation difference between two individual models of static surfaces (Dai and Howat, 2017).

3.3 Assimilation setup

We recall that our aim is to initialise the model using the DA framework to estimate the state together with the basal conditions. As a simplification to realistic experiments, we assume in the following that the ice rheological properties (represented by the

Glen flow law and its parameter) and the forcing (represented by the surface and basal mass balances in Eq. (4)) are perfectly known. In addition, we assume that the form of the basal friction follows Eq. (3) with $m = 1/3$, so that only the spatially-varying friction coefficient C is uncertain.

In our model, as the force balance equation (1) contains no time derivative, the velocity is a diagnostic variable. Because
5 of the flotation condition, the topography can be represented by only one prognostic variable. The state vector $\boldsymbol{x}$ is then given by the free surface elevation z_s at every mesh node. The state vector is augmented by the two parameters to be estimated, the bedrock topography b and the basal friction coefficient C. Because the velocities are insensitive to the basal conditions where ice is floating, these two parameters are included in the state vector only for the nodes where at least one member is grounded. In addition, to insure that C remains positive, we use the following change of variable for the assimilation $C = \alpha^2$.
10 As the synthetic bed observations are used to construct the initial ensemble (cf next section), we assimilate only the surface elevation and velocity observations, every year from $t = 1\,\mathrm{a}$ up to $t = 35\,\mathrm{a}$. The observation operator H is a simple mapping for the surface elevation, and is given by the non-linear SSA equation (Eq. 1) for the surface velocities.

Finally, to illustrate the effect of the transient assimilation on model projections on time scales relevant for sea level projections, the analysed states at $t = 20\,\mathrm{a}$ and $t = 35\,\mathrm{a}$ are used to run deterministic and ensemble forecasts up to $t = 200\,\mathrm{a}$.
15 The deterministic forecast uses the ensemble mean produced by the analysis while the ensemble forecast propagates the full ensemble.

3.4 Initial ensemble

The initial ensemble must reflect the background and the estimation of its uncertainty, available *a priori* before the assimilation. Kalman-based filters are based on the hypothesis of the independence between the background and the observations that are
20 used during the assimilation.

For the bed, we use the synthetic observations to draw conditional Gaussian simulations using the R package *gstat* (Pebesma and Wesseling, 1998). To model the spatial dependence, we use an exponential function for the variogram with a range of $50\,\mathrm{km}$, a sill of $4000\,\mathrm{m}^2$ and a nugget of $200\,\mathrm{m}^2$. For a large ensemble, the ensemble mean should converge to the prediction obtained by kriging. The ensemble mean and spread for a 50-members ensemble are shown in Fig. 2 and the first three members
25 are shown in Fig. 3. As expected, the ensemble spread increases with the distance from the observations. At the observation locations, the spread is controlled by the nugget which is meant to represent the bed measurement error. However, for the individual members, the nugget controls the small scale variability, resulting in a roughness larger than the reference. When averaged this roughness disappears, and the ensemble mean has a much smoother topography.

For the friction coefficient, we assume that we know the mean value $C_{mean} = 0.020\,\mathrm{MPa\,m}^{-\frac{1}{3}}\,\mathrm{a}^{-\frac{1}{3}}$ and draw unconditional
30 simulations. For the spatial dependence, we use a Gaussian function for the variogram using a range of $2.5\,\mathrm{km}$, and a sill of $8.10^{-5}\,\mathrm{MPa}^2\,\mathrm{m}^{-\frac{2}{3}}\,\mathrm{a}^{-\frac{2}{3}}$. This results in initial ensemble members that have approximately the same maximal amplitude as the reference, as shown in Fig. 3.

For the free surface, we initialise all the members using the observed (noisy) free surface at $t = 0$. Doing so, we implicitly assume that the spread of the ensemble induced by the uncertain initial conditions at the first analysis is small compared to the

spread induced by the uncertain parameters. This is motivated by the fact that divergence anomalies induced by uncertainties in model parameters can typically reach tens to hundreds of meters per years in fast flowing areas (Seroussi et al., 2011).

4 Results

4.1 Assimilation

5 To assess the performance of the DA in retrieving the basal conditions we compute the root-mean-square error (RMSE) between the analysed ensemble mean and the reference for both the bed and the friction coefficient, RMSE_b and RMSE_C respectively. After each analysis, the RMSE is computed using all the nodes where the basal conditions have been updated by the assimilation, i.e. at least one member is grounded, and where $x \geq 300\,\mathrm{km}$. The later value is close to the position reached by the grounding line after 200 years in the reference simulation, moreover, during the assimilation window, the reference velocity at

10 this location is close to $80\,\mathrm{m\,a^{-1}}$ (Fig. 4), so that the relative noise is $\sim 25\%$ and we don't expect too much improvement from the DA upstream as the velocity tends to 0.

Here the size of the state vector $\boldsymbol{x}$ is approximately 8400, *i.e.* z_s at every node and the basal conditions, b and C, in the grounded part. To test the performances of DA in conditions that would be numerically affordable for real applications, we run the assimilation with relatively small ensemble sizes $N_e = 30$, $N_e = 50$ and $N_e = 100$. In this case, inflation and localisation

15 are required to counteract the effects of undersampling and we test a range of forgetting factors ρ and localisation radius r. The errors obtained at $t = 20\,\mathrm{a}$ relative to the errors from the initial ensemble mean are shown in Fig. 5. The performances of the assimilation for $N_e = 50$ and $N_e = 100$ are very similar. The filter diverges and produces errors larger than the initial errors for a localisation radius $r \leq 4\,\mathrm{km}$. However, for larger localisation radii, the assimilation is relatively robust for a wide range of r and ρ, with errors reduced by $\sim 30\%$ for b and $\sim 40\%$ for C. Decreasing the ensemble sizes reduces the filter performance but

20 there is still a reduction of the errors by $\sim 20\%$ and $\sim 30\%$, respectively, with $N_e = 30$. For the two smallest ensembles, there is an optimal value for r and increasing r above this value decreases the filter performance. In general, this optimal value for r increases as ρ decreases, because the ensemble spread reduction induced by assimilating more observations is counterbalanced by the inflation.

In the sequel we discuss the results obtained with an ensemble size $N_e = 50$. As a compromise between the performances in retrieving b and C, we choose a forgetting factor $\rho = 0.92$ and a localisation radius $r = 8\,\mathrm{km}$. The evolution of the RMSEs

25 as a function of assimilation time together with the initial and final ensembles are shown in Fig. 2. RMSE_b decreases steadily from $\sim 25\,\mathrm{m}$ for the initial ensemble at $t = 0$ to $\sim 12\,\mathrm{m}$ at $t = 35\,\mathrm{a}$. For the basal friction, RMSE_C is decreased by a factor 1.75 during the first ten years, then there is still a slight but much smaller improvement as new observations are assimilated.

At the end of the assimilation, for both fields, the spatial variations are well reproduced by the ensemble mean and, compared to the initial ensemble, the difference from the reference is decreased everywhere except between 300 and $325\,\mathrm{km}$ for C. The

30 reduction in the error is also accompanied by a diminution of the ensemble spread, represented by the minimum and maximum values in Fig. 2. This reduction is the most important just upstream of the grounding line where the relative noise for the velocity is the smallest. For the first $100\,\mathrm{km}$ upstream of the grounding line, the ensemble standard deviation increases by a

factor 4, from approximately 4 to $17\,\mathrm{m}$ for b and from 1.10^{-3} to $4.10^{-3}\,\mathrm{MPa\,m^{-\frac{1}{3}}\,a^{-\frac{1}{3}}}$ for C. Downstream of the GL where all members are floating, the model is insensitive to the basal conditions and the initial ensemble is unchanged.

Figure 1 shows that some members undergo a fast GL retreat of few kilometres before assimilation at the end of the first year. Interestingly, as the assimilation updates both the thickness and the bed, it also corrects the GL position which never

5   departs by more than few nodes from the reference for the rest of the assimilation period.

As in realistic simulations, the true bed and friction are not available to assess the performance of the DA, we also look at the variables assimilated by the model. Figure 6 shows the RMSEs between the ensemble mean and the reference for the velocity u (RMSE_u) and the free surface zs (RMSE_{z_s}), computed for the entire domain ($0 \leq x \leq 800\,\mathrm{km}$). We also report the evolution of the ensemble spread, computed as the square root of the averaged ensemble variance. The velocities before and after the

10   analysis at $t = 1\,\mathrm{a}$ and $t = 35\,\mathrm{a}$ are shown in Fig. 4. The RMSEs are largely decreased during the first few years, especially for the velocity with an error of more than $300\,\mathrm{m\,a^{-1}}$ before the first assimilation to approximately the noise level, $20\,\mathrm{m\,a^{-1}}$, at $t = 20\,\mathrm{a}$. For zs, RMSE_{z_s} is already below the noise level before the first analysis and decreases relatively steadily to reach $\sim 2\,\mathrm{m}$ after 35 years. RMSE_u increases at the end of the period when the reference GL leaves the stable region. As can be shown in Fig. 4, the error is dominated by the larger difference over the ice-shelf due to the few members that still have their

15   GL at the stable location, largely affecting the ensemble mean.

In general, during the first and last years of the assimilation period, the error and the ensemble spread increase during the forecast step. The analysis step reduces both the error and the ensemble spread (Fig. 6). With the stabilisation of the grounding line, both the error and the spread remain relatively stable during the forecast, and as RMSE_u and RMSE_{z_s} have already reached levels comparable to the observation noise, there is no much improvement during the analysis. After few assimilation

20   steps, as expected for a reliable ensemble, the error and the spread have similar values.

4.2   forecast simulations

We now discuss model projections from the initial state to $t = 200\,\mathrm{a}$.

Without assimilation, the deterministic forecast, i.e. using the ensemble mean basal conditions, rapidly leads to the fastest GL retreat and, after few years the GL position is no more included within the previsions from the ensemble (Fig.1B). This is due

25   to the fact that the ensemble mean is smoother than the reference and any of the ensemble members. The reference GL position is included in the ensemble and at the end of the simulations most of the members are within $\pm 25\,\mathrm{km}$ from the reference. However, for few members the GL remains very stable near its initial position for tens to hundreds of years, eventually never switching to an unstable regime during the duration of the simulation. Retreat rates are relatively variable from one member to the other, depending on the basal conditions.

30   With assimilation, the ensemble mean is improved and the difference from the reference reduced. The deterministic forecast cannot be distinguished from the ensemble members any more (Fig.1C-D). Retreat rates are closer to the reference, with the previsions from all the ensemble members being more or less parallel to the reference. We note however that, when the forecast starts after an assimilation window of 20 years, i.e. during a period of stable GL position for the reference, the deterministic forecast leaves the stable position with a delay of approximately 25 years, and a few members remain stable for the entire

simulation. On average between t=13 to t=32 a, the thinning rate at the GL in the reference simulation, is approximately 0.6 m/a, reducing to 0.25 m/a during the last two years. The total thinning between two analyses is then much lower than the noise in the observed surface elevation and cannot be captured accurately by the DA. In addition, at the GL, the difference between the minimum and maximum bed elevation given by the ensemble is approximately 20 meters. This remaining uncertainty

5   induces a difference of more than two meters for the floatation surface, and combined with the small thinning rates explains the delays in the initiation of the instability.

Extending the assimilation window up to $t = 35\,\mathrm{a}$ when the reference has switched in a fast retreat, allows to force all the members in the unstable retreat. There is a very good agreement between the reference and the deterministic forecast up to $t = 110\,\mathrm{a}$. This is also true for the ensemble and after that the spread is larger and the predicted GLs are less retreated than for

10   the reference.

5 Discussion

Here, we have tested an ensemble Kalman Filter to assimilate annually observed surface velocities and surface elevation in a marine ice-sheet model. Similarly to previous studies, we have shown that, in fast flowing regions, it is possible to accurately separate and recover both the basal topography and basal friction from surface observations (Gudmundsson and Raymond,

15   2008; Goldberg and Heimbach, 2013; Bonan et al., 2014; Mosbeux et al., 2016). In view of our results, because the synthetic bed observations were already used once to generate the initial ensemble, it seems unnecessary to assimilate these same observations again during each analysis as in Bonan et al. (2014).

Using a scheme that assimilates time-dependent observations provides a model state consistent with transient changes and that can directly serve as an optimal initial condition to run forecast simulations without the need of an additional relaxation

20   (Goldberg and Heimbach, 2013; Goldberg et al., 2015). Interestingly the position of the grounding line is also corrected during the analysis step, and the ensemble quickly converges within few grid nodes from the reference. In addition, the ensemble framework naturally allows to estimate and propagate the uncertainty of the estimated parameters. We have shown that the remaining uncertainties in the basal conditions do not significantly affect GL retreat rates once the unstable retreat is engaged but can lead to considerable delays in the initiation of the instability.

25   Contrary to the variational methods that require the linearisation of the forward model and the computation of the adjoint, the DA framework presented here is fairly independent of the ice flow model. This in an advantage with models that are still relatively young, continuously under development and with a variety of applications and configurations that can use different force balance approximations and parametrisations.

In the experiments presented above, we have used a depth integrated model for the force balance equations where GL

30   migration is implemented through a hydrostatic floatation condition. This allows to fully describe the ice topography with only one prognostic variable. Adaptation of the framework to a full-Stokes model requires minimum adaptations, however these models do not rely on the floatation condition and solve a proper contact problem for the grounding line migration (Durand et al., 2009), this implies to incorporate the two prognostic free surfaces z_b and z_s in the state vector. These models might be

more sensitive to unbalanced geometries that could result from the analyses, especially when localisation is used (Cohn et al., 1998; Houtekamer and Mitchell, 2001). However, the ESTKF, as the ETKF, induces a minimal transformation of the ensemble members and thus has better chances to preserve balance (Nerger et al., 2012).

If the implementation is not an issue, the computational cost implied by running a full-Stokes model might remain a limiting

5 factor. Compared to the Stokes solution, the SSA is known to overestimates the effects of bed topography perturbations on the surface profile for wavelengths less than few ice thicknesses (Gudmundsson, 2008). How this issue can affect the reconstruction of the basal properties has never been quantified, however snapshot basal friction inversions have shown that the solution is sensitive to the force balance approximation (Morlighem et al., 2010). In addition, the MISMIP experiments have shown that the GL position and its response to a perturbation depend on the force balance solved by the models (Pattyn et al., 2012, 2013).

10 In real applications, the performance of EnKFs can be improved by explicitly taking into account the model error. Several strategies have been developed to account for this error, one approach being to use different versions of the model for different ensemble members (Houtekamer et al., 2009). Further studies could investigate the potential benefits of using ensembles that combine several force balance approximations.

Before generalizing such methods to real glacial systems, three points must be taken in consideration. They are independent

15 of the DA method but they will eventually be treated differently in a variational or in an ensemble framework.

First, the quality of the analysis and the accuracy of the error estimates depends on the observation error covariance matrix $\mathbf{R}$. It is then important to provide meaningful error estimates. Recent velocity maps provide an error estimates reported as the 1σ value for each individual location (Mouginot et al., 2012; Joughin et al., 2018). In general, this value agrees well with independent estimates, however care must be taken when the maps results from a composite of different sensors or different

20 periods.

Second, the results depends on prior assumptions on the control variables and their variability, represented here by the initial ensemble. For the basal topography, current reference maps provide local error estimates (Fretwell et al., 2013; Morlighem et al., 2017), however they do not provide informations about spatial correlations so that generating initial ensembles with the correct statistics might be problematic. In addition, the gridding can result in a loss of information for some regions of

25 dense measurements, or can lead to too smooth terrains in sparsely sampled areas. With the aim of generating terrains that have the correct high-resolution roughness, Graham et al. (2017) propose a synthetic 100-m resolution Antarctic bed elevation that combines the reference topography bedmap2 (Fretwell et al., 2013) with an unconditional simulation where the spatial correlation is fitted from dense radar measurements. This method could be used to generate initial ensembles but requires to have access to the initial high resolution measurements. Generating initial ensembles for the basal friction might be more

30 problematic as there is in general no independent *a-priori* informations about the magnitude and spatial variability of the basal friction. If there is a correlation between the basal drag and the seismic observations of the bed conditions at large scale, a proper physical theory is still missing to quantitatively incorporate such informations in the models (Kyrke-Smith et al., 2017). It could be interesting to investigate how the existing multi-model basal friction reconstructions, based on snapshot inversions, could be used to derive initial uncertainty statistics and reduce the initial ensemble spread.

35 Finally, in our synthetic applications, we have not accounted for all potential sources of uncertainty which are, for example:

- the ice flow law: the ice viscosity depends on the englacial temperature which itself is function of the ice sheet history and the boundary forcing, including the geothermal heat flux (e.g. Van Liefferinge and Pattyn, 2013). Several other processes also affect the ice viscosity, including damage and strain-induced mechanical anisotropy (e.g. Pimienta et al., 1987; Schulson and Duval, 2009; Borstad et al., 2013). For the stress exponent, if the values $n = 3$ is used by most models, published values ranges between 1 and 5 (e.g. Gillet-Chaulet et al., 2011).

- The friction law: more and more direct or indirect evidences show that the friction under fast ice streams is at least partially controlled by the presence of sediments leading to a Coulomb type friction law (e.g. Tulaczyk et al., 2000; Murray, 1997; Joughin et al., 2010; Gillet-Chaulet et al., 2016). For hard beds, the development of subglacial cavities also implies deviations for the classical Weertman friction law (Schoof, 2005; Gagliardini et al., 2007).

- The density: the firn layer is not accounted for in most models, however its depth and density affect the floatation condition and thus the GL position (e.g. Griggs and Bamber, 2011). Direclty assimilating the GL position, using *e.g.* the moving mesh approach develop by Bonan et al. (2017), would certainly be beneficial in realistic applications to reduce the discrepancy between the modelled and observed GL (Goldberg et al., 2015).

- The external forcings from the atmosphere and the ocean:increasing mass loss rates from the ice sheets, in a large portion, can be attributed to a response to oceanic forcing, but multiple challenges remain for a proper assessment of their magnitude (Joughin et al., 2012).

Realistic simulations with ice flow models cover a wide range of spatial and temporal scales, and the relative importance of these uncertainties as well as their representation in the models will certainly have to be evaluated partly in a case by case basis, requiring to develop robust framework for a variety of applications.

6 Conclusions

Developing model initialisation strategies that properly reproduce the ice-sheets dynamical mass losses observed over the last decades, requires to develop transient assimilation frameworks that are able to account for the growing availability of dense time series, especially from space observations. Here, we presented a synthetic twin experiment demonstrating the possibility to calibrate a marine ice model using an ensemble Kalman Filter which requires less numerical developments than variational methods.

Using resolutions and noise levels consistent with current observing systems, good performances are obtained to recover both the basal friction and basal topography with an ensemble of at least 50 members. Localisation and inflation have been tuned manually, however the results are consistent over relatively wide ranges. Future studies should investigate how these values can be transposed to realistic applications. Nevertheless, there is an abundant and growing literature in other geophysical fields to overcome problem that we might be facing in future studies.

Once the GL enters an unstable region, retreat rates largely depends on the basal conditions, thus using DA to reduce the associated uncertainties largely increases the skill of the model to predict rates and magnitude of GL retreat for time scales

relevant for sea level rise projections. In our simplified application, the assimilation of the surface observations was sufficient to capture the GL migration during the assimilation window, without explicitly assimilating the observed position. However, for the GL to enter a irreversible retreat, the thickness must reach a tipping point, *i.e.* the thickness at the GL must reach floatation. This can seriously impact the predictability of the system as, for small perturbations, remaining uncertainties on the

5   basal conditions can lead to an uncertainty on the residence time of the GL on stabilisation points, that can be similar to the simulation timescale.

Finally, we have discussed the main challenges to tackle before generalizing transient DA in ice-sheet modelling. This includes a better assessment of the uncertainties in the model and in the observations used for the background and for the assimilation.

10 *Code availability.* Elmer/Ice code is publicly available through GitHub (https://github.com/ElmerCSC/elmerfem, Gagliardini et al. (2013)). PDAF is distributed under the GNU General Public License, version 3, and is available at http://pdaf.awi.de.

Competing interests. The authors declare that they have no competing interests.

Acknowledgements. This work was funded by the French National Research Agency (ANR) through the TROIS-AS (ANR-15-CE01-0005-01). The author thanks G. Durand, O. Gagliardini and J. Mouginot for valuable comments on the first drafts of the manuscript.

References

Bannister, R. N.: A review of operational methods of variational and ensemble-variational data assimilation: Ensemble-variational Data Assimilation, Quarterly Journal of the Royal Meteorological Society, 143, 607–633, https://doi.org/10.1002/qj.2982, 2017.

Bishop, C. H., Etherton, B. J., and Majumdar, S. J.: Adaptive Sampling with the Ensemble Transform Kalman Filter. Part I: Theoretical
5 Aspects, Monthly Weather Review, 129, 420–436, https://doi.org/10.1175/1520-0493, 2001.

Bonan, B., Nodet, M., Ritz, C., and Peyaud, V.: An ETKF approach for initial state and parameter estimation in ice sheet modelling, Nonlin. Processes Geophys., 21, 569–582, 2014.

Bonan, B., Nichols, N. K., Baines, M. J., and Partridge, D.: Data assimilation for moving mesh methods with an application to ice sheet modelling, Nonlin. Processes Geophys., 24, 515–534, https://doi.org/10.5194/npg-24-515-2017, 2017.

10 Borstad, C. P., Rignot, E., Mouginot, J., and Schodlok, M. P.: Creep deformation and buttressing capacity of damaged ice shelves: theory and application to Larsen C ice shelf, The Cryosphere, 7, 1931–1947, https://doi.org/10.5194/tc-7-1931-2013, 2013.

Brondex, J., Gagliardini, O., Gillet-Chaulet, F., and Durand, G.: Sensitivity of grounding line dynamics to the choice of the friction law, J. Glaciol., 63, 854–866, https://doi.org/10.1017/jog.2017.51, 2017.

Brondex, J., Gillet-Chaulet, F., and Gagliardini, O.: Sensitivity of centennial mass loss projections of the Amundsen basin to the friction law,
15 The Cryosphere, 13, 177–195, https://doi.org/10.5194/tc-13-177-2019, 2019

Church, J. A., Clark, P. U., Cazenave, A., Gregory, J. M., Jevrejeva, S., Levermann, A., Merrifield, M. A., Milne, G. A., Nerem, R. S., Nunn, P. D., Payne, A. J., Pfeffer, W. T., Stammer, D., and Unnikrishnan: Sea level change, in: Climate Change 2013: The Physical Science Basis. Contribution of Working Group I to the Fifth Assessment Report of the Intergovernmental Panel on Climate Change, [Stocker, T.F., D. Qin, G.-K. Plattner, M. Tignor, S.K. Allen, J. Boschung, A. Nauels, Y. Xia, V. Bex and P.M. Midgley (eds.)], Cambridge University
20 Press, Cambridge, United Kingdom and New York, NY, USA., 2013.

Cohn, S. E., da Silva, A., Guo, J., Sienkiewicz, M., and Lamich, D.: Assessing the Effects of Data Selection with the DAO Physical-Space Statistical Analysis System*, Monthly Weather Review, 126, 2913–2926, https://doi.org/10.1175/1520-0493, 1998.

Dai, C. and Howat, I. M.: Measuring Lava Flows With ArcticDEM: Application to the 2012-2013 Eruption of Tolbachik, Kamchatka, Geophys. Res. Lett., 44, 12,133–12,140, https://doi.org/10.1002/2017GL075920, 2017.

25 Durand, G. and Pattyn, F.: Reducing uncertainties in projections of Antarctic ice mass loss, The Cryosphere, 9, 2043–2055, https://doi.org/10.5194/tc-9-2043-2015, 2015.

Durand, G., Gagliardini, O., Zwinger, T., Le Meur, E., and Hindmarsh, R. C.: Full Stokes modeling of marine ice sheets: influence of the grid size, Annals Glaciol., 50, 109–114, https://doi.org/10.3189/172756409789624283, 2009.

Durand, G., Gagliardini, O., Favier, L., Zwinger, T., and Meur, E. l.: Impact of bedrock description on modeling ice sheet dynamics, Geophys.
30 Res. Lett., 38, https://doi.org/201110.1029/2011GL048892, 2011.

Enderlin, E. M., Howat, I. M., and Vieli, A.: High sensitivity of tidewater outlet glacier dynamics to shape, The Cryosphere, 7, 1007–1015, https://doi.org/10.5194/tc-7-1007-2013, 2013.

Evensen, G.: Sequential data assimilation with a nonlinear quasi-geostrophic model using Monte Carlo methods to forecast error statistics, J. Geophys. Res., 99, 10 143, https://doi.org/10.1029/94JC00572, 1994.

35 Fretwell, P., Pritchard, H. D., Vaughan, D. G., Bamber, J. L., Barrand, N. E., Bell, R., Bianchi, C., Bingham, R. G., Blankenship, D. D., Casassa, G., Catania, G., Callens, D., Conway, H., Cook, A. J., Corr, H. F. J., Damaske, D., Damm, V., Ferraccioli, F., Forsberg, R., Fujita, S., Gim, Y., Gogineni, P., Griggs, J. A., Hindmarsh, R. C. A., Holmlund, P., Holt, J. W., Jacobel, R. W., Jenkins, A., Jokat, W., Jordan,

T., King, E. C., Kohler, J., Krabill, W., Riger-Kusk, M., Langley, K. A., Leitchenkov, G., Leuschen, C., Luyendyk, B. P., Matsuoka, K., Mouginot, J., Nitsche, F. O., Nogi, Y., Nost, O. A., Popov, S. V., Rignot, E., Rippin, D. M., Rivera, A., Roberts, J., Ross, N., Siegert, M. J., Smith, A. M., Steinhage, D., Studinger, M., Sun, B., Tinto, B. K., Welch, B. C., Wilson, D., Young, D. A., Xiangbin, C., and Zirizzotti, A.: Bedmap2: improved ice bed, surface and thickness datasets for Antarctica, The Cryosphere, 7, 375–393, https://doi.org/10.5194/tc-7-375-2013, 2013.

Gagliardini, O., Cohen, D., Råback, P., and Zwinger, T.: Finite-element modeling of subglacial cavities and related friction law, J. Geophys. Res., 112, https://doi.org/10.1029/2006JF000576, 2007.

Gagliardini, O., Zwinger, T., Gillet-Chaulet, F., Durand, G., Favier, L., de Fleurian, B., Greve, R., Malinen, M., Martín, C., Råback, P., Ruokolainen, J., Sacchettini, M., Schäfer, M., Seddik, H., and Thies, J.: Capabilities and performance of Elmer/Ice, a new-generation ice sheet model, Geosci. Model Dev. 6, 1299–1318, https://doi.org/10.5194/gmd-6-1299-2013, 2013.

Gaspari, G. and Cohn, S. E.: Construction of correlation functions in two and three dimensions, Quarterly Journal of the Royal Meteorological Society, 125, 723–757, https://doi.org/10.1002/qj.49712555417, 1999.

Gillet-Chaulet, F., Hindmarsh, R. C. A., Corr, H. F. J., King, E. C., and Jenkins, A.: In-situ quantification of ice rheology and direct measurement of the Raymond Effect at Summit, Greenland using a phase-sensitive radar, Geophys. Res. Lett., 38, https://doi.org/201110.1029/2011GL049843, 2011.

Gillet-Chaulet, F., Gagliardini, O., Seddik, H., Nodet, M., Durand, G., Ritz, C., Zwinger, T., Greve, R., and Vaughan, D. G.: Greenland ice sheet contribution to sea-level rise from a new-generation ice-sheet model, The Cryosphere, 6, 1561–1576, https://doi.org/10.5194/tc-6-1561-2012, 2012.

Gillet-Chaulet, F., Durand, G., Gagliardini, O., Mosbeux, C., Mouginot, J., Rémy, F., and Ritz, C.: Assimilation of surface velocities acquired between 1996 and 2010 to constrain the form of the basal friction law under Pine Island Glacier, Geophys. Res. Lett., 43, 2016GL069 937, https://doi.org/10.1002/2016GL069937, 2016.

Gladstone, R. M., Payne, A. J., and Cornford, S. L.: Resolution requirements for grounding-line modelling: sensitivity to basal drag and ice-shelf buttressing, Annals Glaciol., 53, 97–105, https://doi.org/10.3189/2012AoG60A148, 2012.

Goldberg, D. N. and Heimbach, P.: Parameter and state estimation with a time-dependent adjoint marine ice sheet model, The Cryosphere, 7, 1659–1678, https://doi.org/10.5194/tc-7-1659-2013, 2013.

Goldberg, D. N., Heimbach, P., Joughin, I., and Smith, B.: Committed retreat of Smith, Pope, and Kohler Glaciers over the next 30 years inferred by transient model calibration, The Cryosphere, 9, 2429–2446, https://doi.org/10.5194/tc-9-2429-2015, 2015.

Goldberg, D. N., Narayanan, S. H. K., Hascoet, L., and Utke, J.: An optimized treatment for algorithmic differentiation of an important glaciological fixed-point problem, Geosci. Model Dev., 9, 1891–1904, https://doi.org/10.5194/gmd-9-1891-2016, 2016.

Graham, F. S., Roberts, J. L., Galton-Fenzi, B. K., Young, D., Blankenship, D., and Siegert, M. J.: A high-resolution synthetic bed elevation grid of the Antarctic continent, Earth Syst. Sci. Data, 9, 267-279, https://doi.org/10.5194/essd-9-267-2017, 2017.

Griggs, J. and Bamber, J.: Antarctic ice-shelf thickness from satellite radar altimetry, J. Glaciol., 57, 485–498, https://doi.org/10.3189/002214311796905659, 2011.

Gudmundsson, G.H. and Raymond, M.: On the limit to resolution and information on basal properties obtainable from surface data on ice streams. The Cryosphere 2, 167—178, 2008.

Gudmundsson, G. H.: Analytical solutions for the surface response to small amplitude perturbations in boundary data in the shallow-ice-stream approximation, The Cryosphere, 2, 77–93, 2008.

Hascoët, L. and Morlighem, M.: Source-to-source adjoint Algorithmic Differentiation of an ice sheet model written in C, Optimization Methods and Software, 33, 829–843, https://doi.org/10.1080/10556788.2017.1396600, 2018.

Houtekamer, P. L. and Mitchell, H. L.: A Sequential Ensemble Kalman Filter for Atmospheric Data Assimilation, Monthly Weather Review, 129, 123–137, https://doi.org/10.1175/1520-0493, 2001.

Houtekamer, P. L., Mitchell, H. L., and Deng, X.: Model Error Representation in an Operational Ensemble Kalman Filter, Monthly Weather Review, 137, 2126–2143, https://doi.org/10.1175/2008MWR2737.1, 2009.

Hunt, B. R., Kostelich, E. J., and Szunyogh, I.: Efficient data assimilation for spatiotemporal chaos: A local ensemble transform Kalman filter, Physica D: Nonlinear Phenomena, 230, 112–126, https://doi.org/10.1016/j.physd.2006.11.008, 2007

Joughin, I., Smith, B. E., and Holland, D. M.: Sensitivity of 21st century sea level to ocean-induced thinning of Pine Island Glacier, Antarctica, Geophys. Res. Lett., 37, https://doi.org/10.1029/2010GL044819, 2010.

Joughin, I., Alley, R. B., and Holland, D. M.: Ice-Sheet Response to Oceanic Forcing, Science, 338, 1172–1176, https://doi.org/10.1126/science.1226481, 2012.

Joughin, I., Smith, B. E., and Howat, I.: Greenland Ice Mapping Project: ice flow velocity variation at sub-monthly to decadal timescales, The Cryosphere, 12, 2211–2227, https://doi.org/10.5194/tc-12-2211-2018, 2018.

Kalnay, E., Li, H., Miyoshi, T., Yang, S.-C., and Ballabrera-Poy, J.: 4-D-Var or ensemble Kalman filter?, Tellus A: Dynamic Meteorology and Oceanography, 59, 758–773, https://doi.org/10.1111/j.1600-0870.2007.00261.x, 2007.

Kyrke-Smith, T.M., Gudmundsson, G.H., Farrell, P.E.: Can Seismic Observations of Bed Conditions on Ice Streams Help Constrain Parameters in Ice Flow Models? J. Geophys. Res.: Earth Surface 122, 2269—2282. https://doi.org/doi.org/10.1002/2017JF004373, 2017

Larour, E., Morlighem, H. S. a. M., and Rignot, E.: Continental scale, high order, high spatial resolution, ice sheet modeling using the Ice Sheet System Model (ISSM), J. Geophys. Res., 117, https://doi.org/201210.1029/2011JF002140, 2012.

Larour, E., Utke, J., Csatho, B., Schenk, A., Seroussi, H., Morlighem, M., Rignot, E., Schlegel, N., and Khazendar, A.: Inferred basal friction and surface mass balance of the Northeast Greenland Ice Stream using data assimilation of ICESat (Ice Cloud and land Elevation Satellite) surface altimetry and ISSM (Ice Sheet System Model), The Cryosphere, 8, 2335–2351, https://doi.org/10.5194/tc-8-2335-2014, 2014.

Larour, E., Utke, J., Bovin, A., Morlighem, M., and Perez, G.: An approach to computing discrete adjoints for MPI-parallelized models applied to Ice Sheet System Model 4.11, Geosci. Model Dev., 9, 3907–3918, https://doi.org/10.5194/gmd-9-3907-2016, 2016.

MacAyeal, D. R.: Large-scale ice flow over a viscous basal sediment: Theory and application to ice stream B, Antarctica, J. Geophys. Res.: Solid Earth, 94, 4071–4087, https://doi.org/10.1029/JB094iB04p04071, 1989.

MacAyeal, D. R.: A tutorial on the use of control methods in ice-sheet modeling, J. Glaciol., 39, 91–98, 1993.

Morlighem, M., Rignot, E., Seroussi, H., Larour, E., Dhia, H. B., and Aubry, D.: Spatial patterns of basal drag inferred using control methods from a full-Stokes and simpler models for Pine Island Glacier, West Antarctica, Geophys. Res. Lett., 37, https://doi.org/10.1029/2010GL043853, 2010.

Morlighem, M., Williams, C. N., Rignot, E., An, L., Arndt, J. E., Bamber, J. L., Catania, G., Chauché, N., Dowdeswell, J. A., Dorschel, B., Fenty, I., Hogan, K., Howat, I., Hubbard, A., Jakobsson, M., Jordan, T. M., Kjeldsen, K. K., Millan, R., Mayer, L., Mouginot, J., Noël, B. P. Y., O'Cofaigh, C., Palmer, S., Rysgaard, S., Seroussi, H., Siegert, M. J., Slabon, P., Straneo, F., van den Broeke, M. R., Weinrebe, W., Wood, M., and Zinglersen, K. B.: BedMachine v3: Complete Bed Topography and Ocean Bathymetry Mapping of Greenland From Multibeam Echo Sounding Combined With Mass Conservation, Geophys. Res. Lett., 44, 11,051–11,061, https://doi.org/10.1002/2017GL074954, 2017.

Mosbeux, C., Gillet-Chaulet, F., Gagliardini, O.: Comparison of adjoint and nudging methods to initialise ice sheet model basal conditions. Geosci. Model Dev. 9, 2549–2562, https://doi.org/10.5194/gmd-9-2549-2016, 2016.

Mouginot, J., Scheuchl, B., and Rignot, E.: Mapping of Ice Motion in Antarctica Using Synthetic-Aperture Radar Data, Remote Sensing, 4, 2753–2767, https://doi.org/10.3390/rs4092753, 2012.

5 Mouginot, J., Rignot, E., Scheuchl, B., and Millan, R.: Comprehensive Annual Ice Sheet Velocity Mapping Using Landsat-8, Sentinel-1, and RADARSAT-2 Data, Remote Sensing 2017, 9(4), , https://doi.org/10.3390/rs9040364, 2017

Murray, T.: Assessing the paradigm shift: deformable glacier beds, Quaternary Science Reviews, 16, 996–1016, 1997.

Nerger, L., Hiller, W., and Schröter, J.: PDAF - The Parallel Data Assimilation Framework: Experiences with Kalman Filtering, in: Use of High Performance Computing in Meteorology, pp. 63–83, WORLD SCIENTIFIC, Reading, UK,
10   https://doi.org/10.1142/9789812701831_0006, 2005.

Nerger, L., Danilov, S., Hiller, W., and Schröter, J.: Using sea-level data to constrain a finite-element primitive-equation ocean model with a local SEIK filter, Ocean Dynamics, 56, 634–649, https://doi.org/10.1007/s10236-006-0083-0, 2006.

Nerger, L., Schröter, J., and Hiller, W.: A Unification of Ensemble Square Root Kalman Filters, Monthly Weather Review, 140, 2335–2345, https://doi.org/10.1175/MWR-D-11-00102.1, 2012.

15 Pattyn, F., Huyghe, A., De Brabander, S., and De Smedt, B.: Role of transition zones in marine ice sheet dynamics, J. Geophysi. Res., 111, https://doi.org/10.1029/2005JF000394,2006.

Pattyn, F., Schoof, C., Perichon, L., Hindmarsh, R. C. A., Bueler, E., de Fleurian, B., Durand, G., Gagliardini, O., Gladstone, R., Goldberg, D., Gudmundsson, G. H., Huybrechts, P., Lee, V., Nick, F. M., Payne, A. J., Pollard, D., Rybak, O., Saito, F., and Vieli, A.: Results of the Marine Ice Sheet Model Intercomparison Project, MISMIP, The Cryosphere, 6, 573–588, https://doi.org/10.5194/tc-6-573-2012, 2012.

20 Pattyn, F., Perichon, L., Durand, G., Favier, L., Gagliardini, O., Hindmarsh, R. C., Zwinger, T., Albrecht, T., Cornford, S., Docquier, D., FüRst, J. J., Goldberg, D., Gudmundsson, G. H., Humbert, A., HüTten, M., Huybrechts, P., Jouvet, G., Kleiner, T., Larour, E., Martin, D., Morlighem, M., Payne, A. J., Pollard, D., RüCkamp, M., Rybak, O., Seroussi, H., Thoma, M., and Wilkens, N.: Grounding-line migration in plan-view marine ice-sheet models: results of the ice2sea MISMIP3d intercomparison, J. Glaciol., 59, 410–422, https://doi.org/10.3189/2013JoG12J129, 2013.

25 Pebesma, E. J. and Wesseling, C. G.: Gstat: a program for geostatistical modelling, prediction and simulation, Computers & Geosciences, 24, 17–31, https://doi.org/10.1016/S0098-3004(97)00082-4, 1998.

Pham, D. T., Verron, J., and Christine Roubaud, M.: A singular evolutive extended Kalman filter for data assimilation in oceanography, Journal of Marine Systems, 16, 323–340, https://doi.org/10.1016/S0924-7963(97)00109-7, 1998.

Pimienta, P., Duval, P., and Lipenkov, V. Y.: Mechanical behavior of anisotropic polar ice, Internationnal Association of Hydrological Sci-
30   ences Publication 170 (Symposium at Vancouver 1987 - Physical Basis of Ice Sheet Modelling), 57–66, 1987

Ritz, C., Edwards, T. L., Durand, G., Payne, A. J., Peyaud, V., and Hindmarsh, R. C. A.: Potential sea-level rise from Antarctic ice-sheet instability constrained by observations, Nature, https://doi.org/10.1038/nature16147, 2015.

Scambos, T., Bell, R., Alley, R., Anandakrishnan, S., Bromwich, D., Brunt, K., Christianson, K., Creyts, T., Das, S., DeConto, R., Dutrieux, P., Fricker, H., Holland, D., MacGregor, J., Medley, B., Nicolas, J., Pollard, D., Siegfried, M., Smith, A., Steig, E., Trusel, L., Vaughan,
35   D., and Yager, P.: How much, how fast?: A science review and outlook for research on the instability of Antarctica's Thwaites Glacier in the 21st century, Global and Planetary Change, 153, 16–34, https://doi.org/10.1016/j.gloplacha.2017.04.008, 2017.

Schoof, C.: The effect of cavitation on glacier sliding, Proc. R. Soc. A, 461, 609–627, https://doi.org/10.1098/rspa.2004.1350, 2005.

Schoof, C.: Marine ice-sheet dynamics. Part 1. The case of rapid sliding, J. Fluid Mech., 573, 27, https://doi.org/10.1017/S0022112006003570, 2007.

Schulson, E. M. and Duval, P.: Creep and Fracture of Ice, Cambridge University Press, 2009.

Seroussi, H., Morlighem, M., Rignot, E., Larour, E., Aubry, D., Dhia, H. B., and Kristensen, S. S.: Ice flux divergence anomalies on 79north
5   Glacier, Greenland, Geophys. Res. Lett., 38, https://doi.org/10.1029/2011GL047338, 2011.

Seroussi, H., Morlighem, M., Larour, E., Rignot, E., and Khazendar, A.: Hydrostatic grounding line parameterization in ice sheet models, The Cryosphere, 8, 2075–2087, https://doi.org/10.5194/tc-8-2075-2014, 2014.

Tsai, V. C., Stewart, A. L., and Thompson, A. F.: Marine ice-sheet profiles and stability under Coulomb basal conditions, J. Glaciol., 61, 205–215, https://doi.org/10.3189/2015JoG14J221, 2015.

10 Tulaczyk, S., Kamb, W. B., and Engelhardt, H. F.: Basal mechanics of Ice Stream B, West Antarctica 1. Till mechanics, J. Geophys. Res., 105, 463–481, 2000.

Van Liefferinge, B. and Pattyn, F.: Using ice-flow models to evaluate potential sites of million year-old ice in Antarctica, Clim. Past, 9, 2335–2345, https://doi.org/10.5194/cp-9-2335-2013, 2013.

Vetra-Carvalho, S., van Leeuwen, P. J., Nerger, L., Barth, A., Altaf, M. U., Brasseur, P., Kirchgessner, P., and Beckers, J.-M.: State-of-the-art
15   stochastic data assimilation methods for high-dimensional non-Gaussian problems, Tellus A: Dynamic Meteorology and Oceanography, 70, 1445 364, https://doi.org/10.1080/16000870.2018.1445364, 2018.

Vieli, A. and Payne, A. J.: Application of control methods for modelling the flow of Pine Island Glacier, West Antarctica, Annals Glaciol., 36, 197–204, 2003.

Vieli, A. and Payne, A. J.: Assessing the ability of numerical ice sheet models to simulate grounding line migration, J. Geophys. Res.: Earth
20   Surface, 110, F01 003, https://doi.org/10.1029/2004JF000202, 2005.
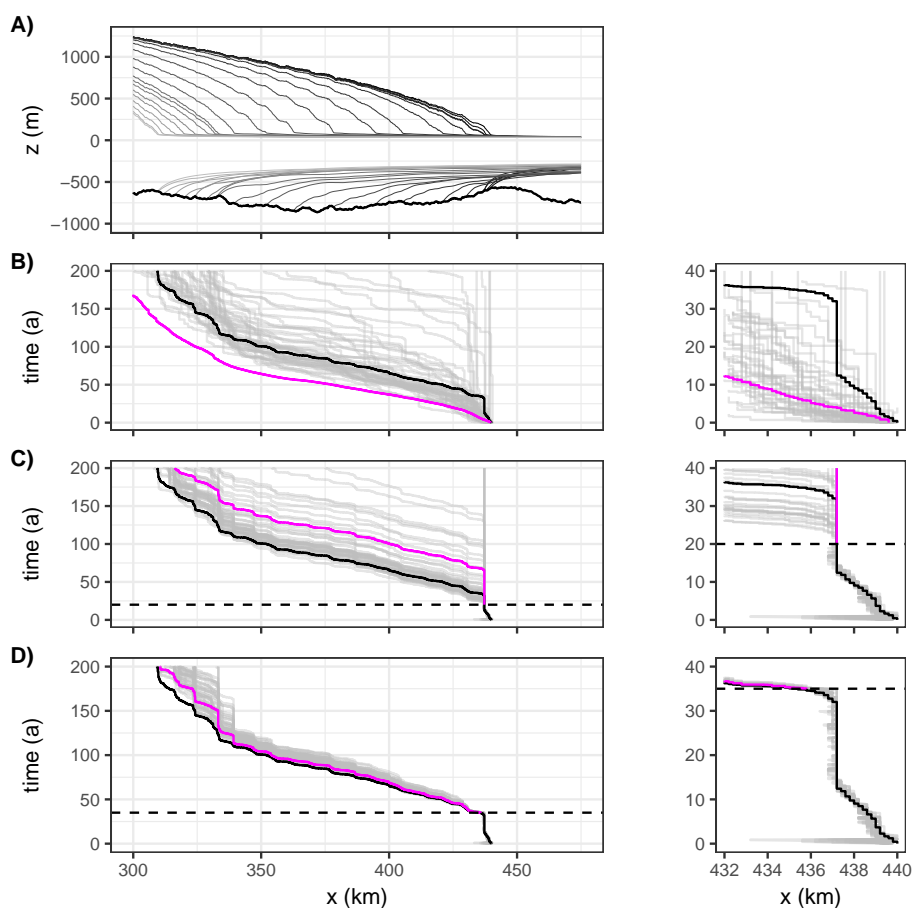
Figure 1. (A) Reference ice sheet topography every 10 years from $t = 0$ to $t = 200\,\mathrm{a}$ (black to grey). (B-D) GL position as a function of the simulation time for the reference (black line), for the ensemble (grey lines), and for the deterministic forecast (magenta line) (B) without assimilation, (C) with assimilation up to $t = 20\,\mathrm{a}$ and (D) with assimilation up to $t = 35\,\mathrm{a}$. The right column show a zoom on the first 40 years. In C-D), the horizontal dashed line show the end of the assimilation window.
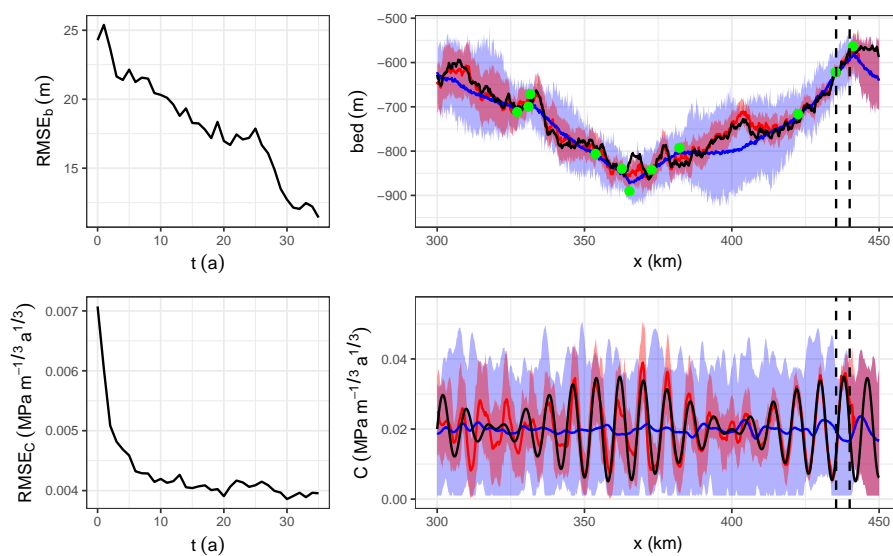
Figure 2. (left) RMSE between the reference and the analysed ensemble mean for the bed and friction coefficient. (Right) Bed and friction coefficient, the reference is shown in black, the synthetic bed measurements in the top panel are shown as green dots, the ensemble mean before assimilation is in blue and at $t = 35\,\mathrm{a}$ in red. The shading shows the ensemble spread between the minimum and maximum values, before assimilation (blue) and at $t = 35\,\mathrm{a}$ (red). The dashed vertical lines show the GL position at $t = 0$ and $t = 35\,\mathrm{a}$.
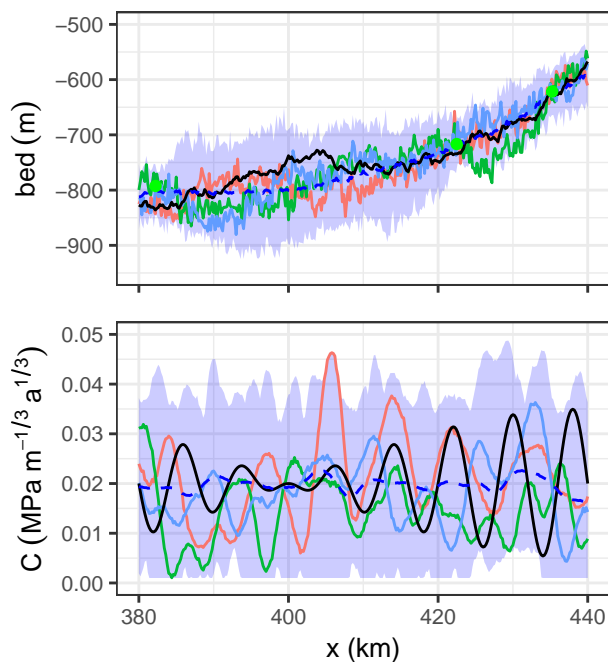
Figure 3. Initial ensemble for the bed and friction coefficient, the reference is shown in black, the synthetic bed measurements are shown as green dots in the top panel, the ensemble mean is the dashed blue curve and the shading shows the ensemble spread. Coloured solid lines show the first 3 members.
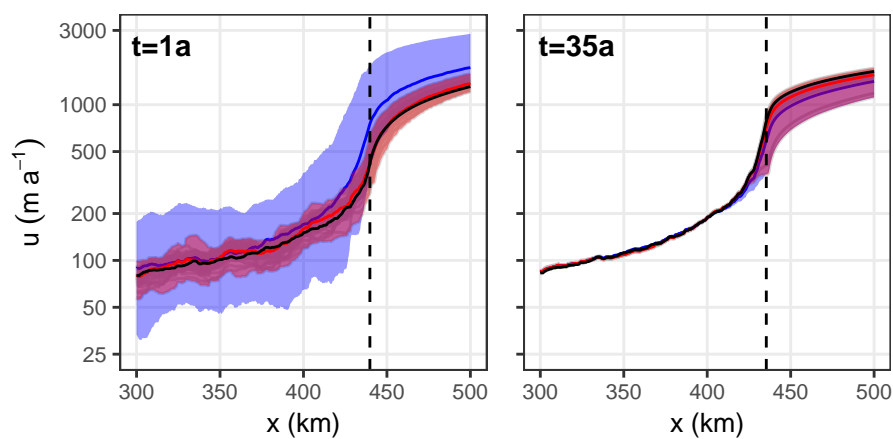
Figure 4. Velocity, u, at $t = 1$a and $t = 35$a. The reference is in black, the ensemble mean before and after the analysis is in blue and red, respectively. The shading shows the ensemble spread between the minimum and maximum. The dashed vertical black indicates grounding line position.
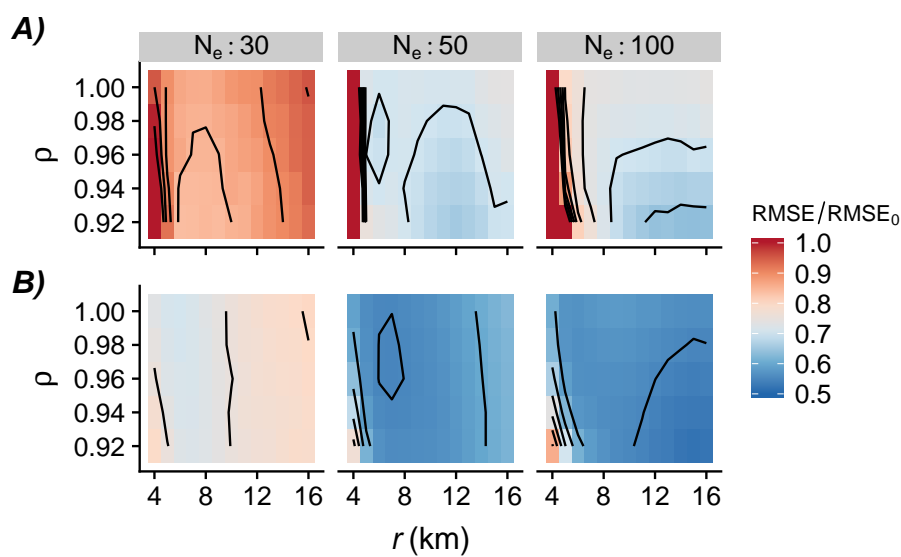
Figure 5. RMSE at $t = 20a$, relative to the initial (before assimilation) RMSE for the 50-member ensemble as a function of the forgetting factor ρ and the localisation radius r for different ensemble sizes N_e. A) for the bed and B) for the friction coefficient. Black lines as isovalues spaced by 5%.
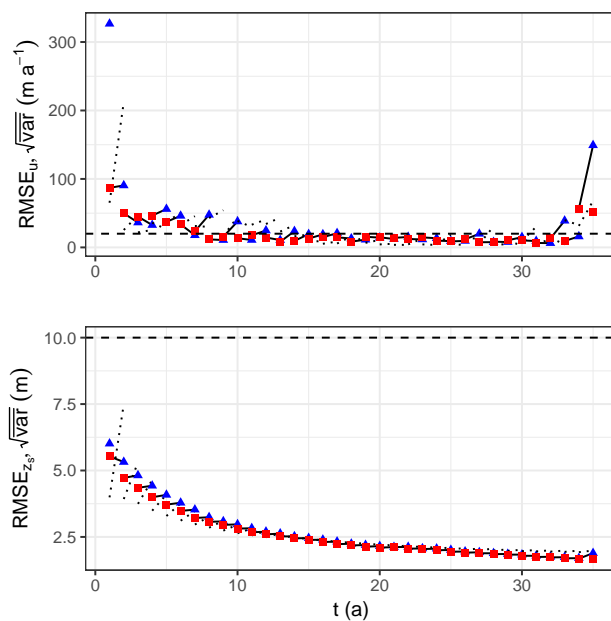
Figure 6. RMSE (solid lines) and square root of the averaged ensemble variance (dashed lines) during the assimilation window for (top) the velocity, u, and (bottom) the free surface, z_s. Each year, the blue triangle and the red square are the RMSEs before and after the analysis, respectively. Each segment represent a 1-year forecast step.